JOURNAL OF THEORETICAL AND APPLIED MECHANICS
62, 4, pp. 737-749, Warsaw 2024
https://doi.org/10.15632/jtam-pl/193391

DYNAMIC CHARACTERISTICS OF ROTOR-SFD SYSTEM WITH INERTIAL EFFECT OF SFD

Zhongyu Yang
Key Laboratory of Light Duty Gas Turbine, Institute of Engineering Thermophysics, Chinese Academy of Sciences, and School of Aeronautics and Astronautics, University of Chinese Academy of Sciences, and National Key Laboratory of Science and Technology on Advanced Light-duty Gas-turbine, Beijing, China

Jiaqi Li
Beijing Aerospace Propulsion Institute, Beijing, China

Jiali Chen
Key Laboratory of Light Duty Gas Turbine, Institute of Engineering Thermophysics, Chinese Academy of Sciences, and School of Aeronautics and Astronautics, University of Chinese Academy of Sciences, and National Key Laboratory of Science and Technology on Advanced Light-duty Gas-turbine, Beijing, China

Yinli Feng
Key Laboratory of Light Duty Gas Turbine, Institute of Engineering Thermophysics, Chinese Academy of Sciences, and National Key Laboratory of Science and Technology on Advanced Light-duty Gas-turbine, Beijing, China, and School of Engineering Sciences, University of Chinese Academy of Sciences
corresponding author Yinli Feng, e-mail: fengyl889@163.com

Squeeze film dampers (SFDs) are damping devices that have been widely used in rotating machines. SFDs can effectively suppress rotor vibration and reduce transmitted forces. This study established a dynamic characteristic model of the SFD considering inertia force and developed the finite element model of the rotor-SFD system by combining fluid mechanics and rotor dynamics. Furthermore, the influence of SFD structural parameters on cavitation, pressure distribution, stiffness, and damping coefficient of the SFD was investigated. The impact of the SFD clearance on the transient dynamic characteristics of the rotor-SFD system was also analyzed.

Keywords: squeeze film damper, inertial effect, rotordynamic

1. Introduction

Squeeze film dampers (SFDs) are widely utilized in aero-engines, gas turbines, steam turbines, etc., owing to their advantages of low cost, simple structure, and outstanding vibration attenuation effect. However, given the inherently nonlinear behavior of an SFD, a poorly designed damper could exacerbate rotor vibrations, significantly influencing the engine operation.

The SFD dynamic characteristics have been extensively investigated via both theoretical and experimental approaches. Gehannin *et al.* (2016) proposed an air ingestion model for SFDs based on the Rayleigh–Plesset equation and investigated the influence of vapor cavitation and air ingestion on the SFD damping characteristics. San Andrés *et al.* (1992) presented an innovative approach for analyzing the dynamic force response of an SFD considering the dynamic flow interaction between the squeeze film lands and the feeding groove. Their model could calculate the corrected values for damping and inertia force coefficients, highlighting the significance of groove volume and the fluid compressibility effect on the dynamic force response of SFDs. Moreover, Zhou *et al.* (2020) developed a three-dimensional model of an SFD considering air

ingestion employing the transient step-size solution method and dynamic mesh technology. They performed model validation through bidirectional excitation experiments. Additionally, they investigated the effects of whirl frequency and eccentricity on air ingestion. Gheller *et al.* (2022) developed a model for SFDs considering both cavitation and inertial forces. Using the finite difference method, they discretized the Rayleigh equation, including the effect of inertial forces, and studied the influence of different boundary conditions on the SFD damping characteristics. Fan *et al.* (2017) developed a cavitation model for SFDs using the Elrod algorithm and Gumbel's cavitation boundary condition, and performed comparisons with commonly used cavitation models. They investigated the influence of fluid inertia effects on the SFD cavitation behavior. Hamzehlouia and Behdinan (2019) used the momentum approximation and perturbation methods to analytically determine the pressure distribution, velocity distribution, and oil film force of SFDs considering lubricant inertia. They developed and experimentally validated a model for SFDs considering lubricant inertia. Drapatow *et al.* (2021) discretized the Navier-Stokes equations considering the local and convective inertia terms using the finite volume method, and they solved for the pressure and oil film reaction of SFDs. Moreover, they investigated the influence of inertial forces on SFD dynamic characteristics under high-temperature and high-speed conditions. Zhou *et al.* (2023) developed a computational fluid dynamics model for a sealed end SFD considering the effects of fluid inertia. They investigated the influence of eccentricity and whirl frequency on stiffness and damping coefficients of an SFD. San Andrés (2014) experimentally determined the dynamic forced response of an SFD with a simplified configuration, where the feedholes were completely eliminated. The measurement results exposed the restricted suitability of classical formulas and distinctly underscored the necessity of employing a more advanced model to precisely forecast the dynamic forced response of practical SFDs.

Chen *et al.* (2017) investigated the relationship between rigid body translation and precession for a rigid rotor-SFD system with nonsymmetric stiffness supports. They considered two cases: precession motion non-resonance and internal resonance when the translation motion was primarily resonant. To establish an optimization model for SFDs, Gupta *et al.* (2023) combined the response surface methodology and analysis of variance. The model considered the influence of journal precession, pressure of oil inlet, and oil-gas mixture ratio on the damping effect of the damper. They optimized SFDs for high-speed rotor systems. Younan *et al.* (2010) investigated the relationship between viscosity and temperature of the lubricating oil, corrected density and viscosity of the lubricating oil, and presented the effect of air pockets. El-Saeidy and Sticher (2010) derived the equation of motion of a system considering nonlinear supports based on the Lagrange equation and investigated dynamic characteristics of elastic support-rotor systems under unbalanced forces. Zapomél *et al.* (2019) proposed a control equation for oil film pressure distribution, solved the equation of motion of a rotor based on the Runge-Kutta method, and revealed nonlinear characteristics stemming from damping. El-Shafei (2002) established a steady-state precession model of the SFD and calculated the pressure distribution of the SFD without seals on both ends.

The traditional SFD models have neglected the influence of fluid inertia forces by assuming that the fluid inertia is completely dominated by viscous forces ($\mathrm{Re} = 0$), and the Reynolds equation has been used to represent the SFD pressure distribution. However, in applications involving high-speed turbomachinery and low-viscosity lubricants, the extrusion Reynolds number in SFDs can exceed one, and thus, the influence of lubricant inertia cannot be neglected (Hamzehlouia and Behdinan, 2019). Although the oil supply system significantly impacts the damping characteristics of SFDs, research on it has been relatively limited. To date, direct research on the influence of SFD clearance, oil inlet parameters, and SFD width on dynamic characteristics of rotors has been lacking. Indeed, most of the aforementioned studies have focused on individual research on SFDs. Hence, this study establishes a numerical model of SFD considering both inertial forces and cavitation. The influence of SFD clearance on cavitation

and damping characteristics are investigated. Moreover, a rotor system model considering SFD is established, and the influence of SFD clearance on the rotor-SFD system is analyzed.

2. Establishment and validation of the dynamic model

2.1. Establishment and validation of the numerical model for a SFD considering inertia

For a rotor system with a SFD, the damping properties of the oil film are crucial. Bearing 1 utilizes a combination of an elastic supporting structure comprising an SFD, a squirrel cage, and a rolling bearing, while bearing 2 adopts a rigid supporting structure with a ball bearing. Figure 1 displays a schematic of the SFD.

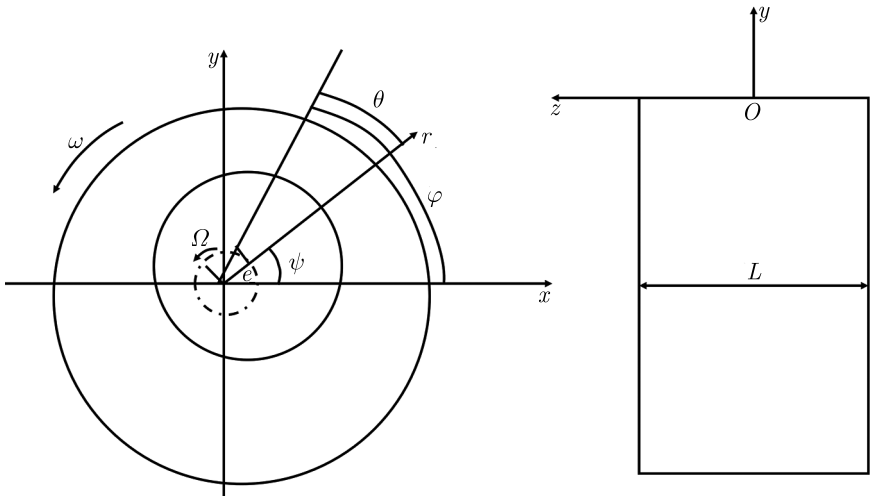

Fig. 1. Schematic of the SFD

To consider the oil film inertia, the axial pressure distribution equation is obtained based on the energy approximations by Crandall and El-Shafei (1991) as follows

$$\begin{aligned} &\frac{\partial p}{\partial z} = z\Big[2\frac{\mu}{h^3}\frac{\partial h}{\partial t} + \frac{6}{5}\frac{\rho}{h}\frac{\partial^2}{\partial t^2} - \frac{102}{35}\frac{\rho}{h^2}\Big(\frac{\partial h}{\partial t}\Big)^2\Big] \\ &p = p_{atm} = 0 \qquad\qquad z = \pm\frac{L}{2} \end{aligned} \tag{2.1}$$

where p is the oil film pressure, ρ is the lubricant density, h is the oil film thickness, μ is the lubricant viscosity, p_{atm} is the atmospheric pressure, and $h = c - e\cos\theta$. Additionally, e is the journal eccentricity, and θ is measured from the positive r-axis of the precessing coordinate system.

The short bearing theory hypothesis is available when no hermetic seals are present at both the ends, and the pressure at both the ends is similar to the external pressure. Due to the squeezing effect, the pressure in the central region of the damper is considerably higher than that at the ends, while the tangential pressure gradient is low

$$\frac{\partial p}{\partial z} \gg \frac{\partial p}{\partial \theta} \qquad p = \Big(\frac{z^2}{2} - \frac{L^2}{4}\Big)\Big[2\frac{\mu}{h^3}\frac{\partial h}{\partial t} + \frac{6}{5}\frac{\rho}{h}\Big(\frac{\partial^2 h}{\partial t^2}\Big) - \frac{102}{35}\frac{\rho}{h^2}\Big(\frac{\partial h}{\partial t}\Big)^2\Big] \tag{2.2}$$

By integrating equation $(2.2)_2$ over the circumferential and axial directions, the radial force F_r and tangential force F_t of the oil film are obtained

$$F_r = -\int_{L/2}^{L/2}\int_{\theta_1}^{\theta_2}(p\cos\theta)R\,d\theta\,dz \qquad F_t = -\int_{L/2}^{L/2}\int_{\theta_1}^{\theta_2}(p\sin\theta)R\,d\theta\,dz \tag{2.3}$$

where R is the SFD housing radius.

The expressions for the equivalent stiffness and equivalent damping coefficients of the SFD are as follows

$$K = -\frac{F_r}{e} \qquad C = -\frac{F_t}{e\Omega} \tag{2.4}$$

The above equations only exemplify the relationship between SFD damping characteristics and the oil film forces. To characterize the influence of inertia forces on vibration reduction characteristics of an SFD, the following dimensionless parameters are given (El-Shafei, 1991)

$$\begin{aligned} f_r &= -C_{rr}\varepsilon' - C_{rt}\varepsilon\psi' - Re\Big(M_{rrad}\varepsilon'' + M_{rnon}\frac{\varepsilon'^2}{\varepsilon} + M_{rtan}\varepsilon\psi'' - M_{rcen}\varepsilon\psi'^2\Big) \\ f_t &= -C_{tr}\varepsilon' - C_{tt}\varepsilon\psi' - Re\Big(M_{trad}\varepsilon'' + M_{tnon}\frac{\varepsilon'^2}{\varepsilon} + M_{ttan}\varepsilon\psi'' - M_{tcen}\varepsilon\psi'^2\Big) \end{aligned} \tag{2.5}$$

where C_{ij} and M_{ij} are the stiffness and inertia coefficients of the oil film force, respectively. $(\cdot') = d/d\tau$, $\tau = \omega t$, and $\varepsilon = e/C$.

The radial oil film force F_r and tangential oil film force F_t are as follows (El-Shafei, 1991)

$$F_r = \frac{\mu\Omega RL^3}{c^2} f_r \qquad F_t = \frac{\mu\Omega RL^3}{c^2} f_t \tag{2.6}$$

Based on the reference (El-Shafei, 1995), the expressions for C_{ij} and M_{ij} are presented in Tables 1 and 2, respectively.

Table 1. Damping coefficient C_{ij}

Damping coefficient of oil film C_{ij}	
$C_{rr} = \dfrac{\pi(1+2\varepsilon^2)}{2(1-\varepsilon^2)^{5/2}}$	$C_{rt} = \dfrac{2\varepsilon}{(1-\varepsilon^2)^2}$
$C_{tr} = \dfrac{2\varepsilon}{(1-\varepsilon^2)^2}$	$C_{tt} = \dfrac{\pi}{2(1-\varepsilon^2)^{3/2}}$

Table 2. Inertial force coefficient M_{ij}

Inertia coefficient of oil film M_{ij}	
$M_{rrad} = \dfrac{\pi}{10\varepsilon^2}[(1-\varepsilon^2)^{-1/2} - 1]$	$M_{tcen} = -\dfrac{27}{70\varepsilon}\Big[2 + \dfrac{1}{\varepsilon}\ln\Big(\dfrac{1-\varepsilon}{1+\varepsilon}\Big)\Big]$
$M_{trad} = -\dfrac{1}{10\varepsilon}\Big[2 + \dfrac{1}{\varepsilon}\ln\Big(\dfrac{1-\varepsilon}{1+\varepsilon}\Big)\Big]$	$M_{rnon} = \dfrac{17\pi}{70\varepsilon^2}\Big[2 - \dfrac{2-3\varepsilon^2}{(1-3\varepsilon^2)^{3/2}}\Big]$
$M_{rtan} = -\dfrac{1}{10\varepsilon}\Big[2 + \dfrac{1}{\varepsilon}\ln\Big(\dfrac{1-\varepsilon}{1+\varepsilon}\Big)\Big]$	$M_{tnon} = \dfrac{17}{70\varepsilon}\Big[2 + \dfrac{2}{\varepsilon}\ln\Big(\dfrac{1-\varepsilon}{1+\varepsilon}\Big) + \dfrac{2}{1-\varepsilon^2}\Big]$
$M_{ttan} = \dfrac{\pi}{10\varepsilon^2}[1 - (1-\varepsilon^2)^{1/2}]$	$M_{rcor} = -\dfrac{1}{70\varepsilon}\Big[20 + \dfrac{27}{\varepsilon}\ln\Big(\dfrac{1-\varepsilon}{1+\varepsilon}\Big) + \dfrac{31}{1-\varepsilon^2}\Big]$
$M_{ren} = \dfrac{\pi}{70\varepsilon^2}\Big[27 - \dfrac{27-17\varepsilon^2}{(1-\varepsilon^2)^{1/2}}\Big]$	$M_{tcor} = \dfrac{\pi}{10\varepsilon^2}\Big[-\dfrac{27}{7} - (1-\varepsilon^2)^{1/2}) + \dfrac{17}{7}\dfrac{2-\varepsilon^2}{(1-\varepsilon^2)^{1/2}}\Big]$

Next, C_{ij} and M_{ij} are substituted into equations (2.5) and (2.6). Then, the expression for the oil film forces considering the influence of the inertia force is

$$F_r = \frac{\mu\Omega r\varepsilon L^3}{c^2}(-C_{rt} + ReM_{rcen}) \qquad F_t = \frac{\mu\Omega r\varepsilon L^3}{c^2}(C_{tt} + ReM_{tcen}) \tag{2.7}$$

The numerical simulation results are validated based on the experimental data from the reference (Zhang, 2018). Table 3 lists the SFD structural parameters.

Table 3. SFD structural parameters

Diameter R [mm]	Clearance C [mm]	Width L [mm]	Eccentricity e	Frequency Ω Ω
43	0.1	18	0.2	80

Table 4 illustrates the comparison between the numerical simulation and experimental results of the SFD. Since the error is less than 5%, the numerical simulation method proposed in this study is considered to be reliable.

Table 4. Comparison between the numerical simulation and experimental results

Coefficient	Experimental	Numerical simulation	Error
Damping [Ns/m]	844	875	3.7%
Stiffness [N/m]	46000	44000	4.3%

2.2. Establishment and validation of the Finite Element model for the rotor system

A finite element model is established for a rotor with an SFD based on the high-pressure rotor of an aviation engine. In this model, the shaft length is 800 mm, the maximum diameter of the shaft is 88 mm, the disk diameter is 160 mm, and the shaft weight is 33 kg. Figure 2 depicts the specific structure of the model. Bearing 1 is a combined elastic support comprising a ball bearing, a squirrel-cage-type elastic support, and an SFD. The stiffness of the elastic support is $5 \cdot 10^6$ N/m. Bearing 2 is a rigid support constituting a roller bearing, with a stiffness of $1 \cdot 10^8$ N/m. Table 5 presents dimensions of each section of the rotor shaft.

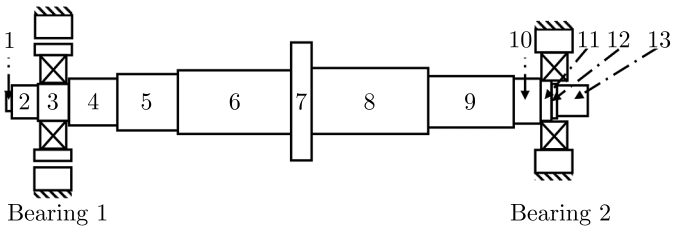

Fig. 2. Specific structure of the rotor-SFD system

Table 5. Dimensions of each section of the rotor shaft [mm]

	No.												
	1	2	3	4	5	6	7	8	9	10	11	12	13
D	25.4	45.5	48	64	76	88	160	86	70	62	57	52	46.5
L	4.5	40	40.5	66	84	158.5	16	170	119	35.5	17	4	45

The Newmark β method is adopted to solve the governing equations of the rotor system (Wang *et al.*, 2022), which can be written as follows

$$M\ddot{\mathbf{q}} + (\mathbf{G} + \mathbf{C})\dot{\mathbf{q}} + \mathbf{K}\mathbf{q} = \mathbf{Q} \tag{2.8}$$

where $\mathbf{M}$ is the mass matrix, $\mathbf{G}$ is the gyro moment matrix, $\mathbf{C}$ is the damping matrix, $\mathbf{K}$ is the stiffness matrix, and $\mathbf{Q}$ is the unbalanced excitation vector.

The damping matrix can be represented using Rayleigh damping

$$\mathbf{C} = \alpha\mathbf{M} + \beta\mathbf{K} \tag{2.9}$$

where α and β are damping coefficients which are related to the modal damping ratio ξ of the structure.

Subsequently, modal dynamic experiments are conducted on the Jeffcott rotor in mounted states to validate the numerical method. Figure 3 exhibits the experimental setup of the mounted modal dynamic testing of the rotor. Figure 4 presents the nodal division for modal dynamic testing of the rotor. The rotor is divided into 13 nodes: node 7 is the pickup point, while the remaining nodes are excitation points.

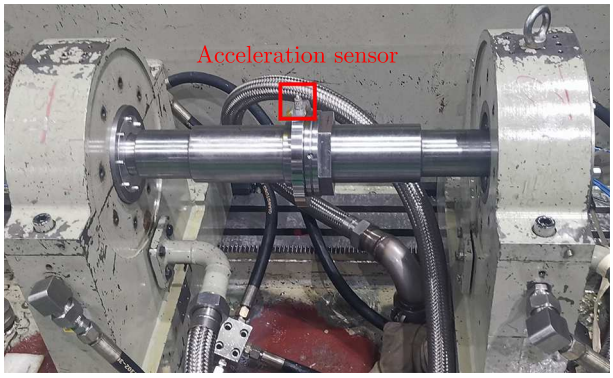

Fig. 3. Experimental setup of the mounted modal dynamic testing

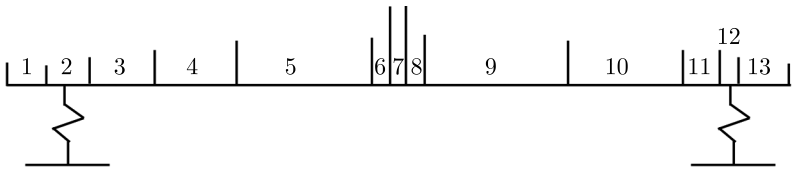

Fig. 4. Nodal division for modal dynamic testing of the Jeffcott rotor

Figure 5 displays the exponential form of transfer function curves for the mounted modal tests. Table 6 illustrates the comparison between the experimental and numerical simulation results for the mounted modal states. Since the mismatch is less than 5%, the numerical simulation results are reliable.

Table 6. Comparison between the experimental and numerical simulation results for the mounted modal state [Hz]

Order	Experiment	Numerical simulation	Error
1st	252	256	1.5%
2nd	1078	1067	1%
3rd	2585	2679	3.6%

Figure 6 depicts the transient experimental setup of the rotor-SFD system. In the system, acceleration sensors are installed at the front and rear bearing positions of the rotor system, while eddy current sensors are placed at the front end, disk, and rear end of the rotor shaft. The system accelerates to 9000 rpm with an acceleration rate of 4.5 rad·s^2.

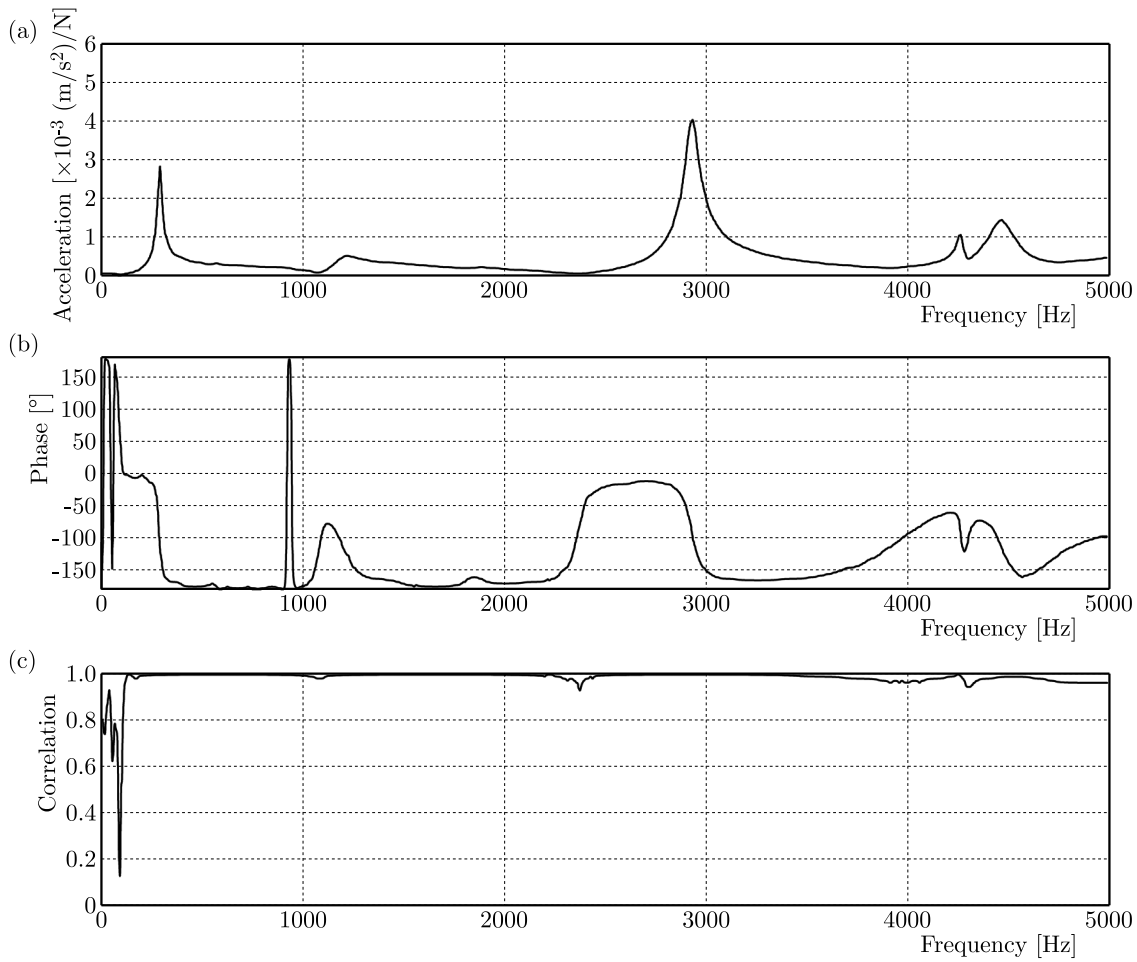

Fig. 5. Exponential form of transfer function curves for the mounted modal test: (a) transfer function curves for the mounted modal tests, (b) phase change, (c) correlation

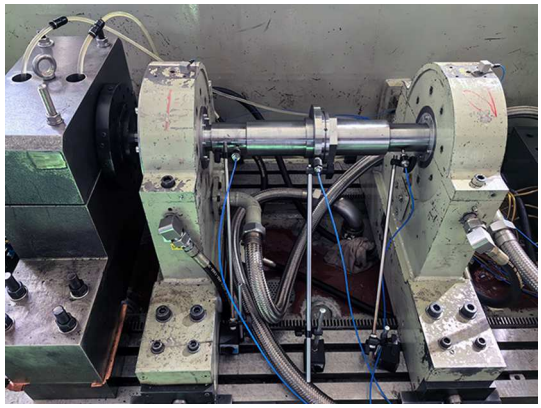

Fig. 6. Transient experimental of the rotor-SFD system

Figure 7 presents the comparison between the experimental and numerical simulation results of the transient acceleration response of the elastic support. The figure shows that compared to the experimental results, the simulation results are smoother with less fluctuations, lower acceleration values, and with an overall error of less than 20%. The simulated results are considered reliable as the experimental environment is unpredictable and complex.

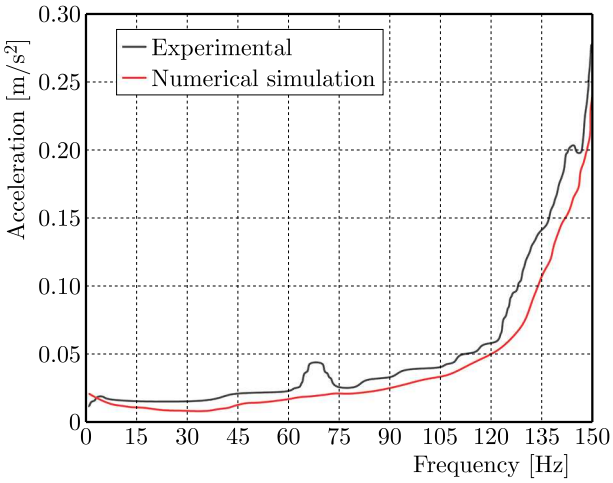

Fig. 7. Transient acceleration response of the rotor system

3. SFD dynamic characteristics

3.1. Cavitation

To investigate the influence of the oil film clearance on cavitation in the SFD, clearances of 0.08, 0.1, 0.12, 0.14, 0.16, 0.18 and 0.2 mm are selected, while the other structural parameters are kept constant.

Figure 8 exhibits the gas phase volume fraction range of the SFDs with different clearances. When the SFD clearance is increased from 0.08 mm to 0.12 mm, both the extent of cavitation and the gas volume fraction decrease. After the SFD clearance exceeds 0.14 mm, the extent of cavitation and the gas volume fraction gradually increase with the clearance. Cavitation includes two phenomena: liquid phase vaporization and air ingestion. Moreover, Figure 9 shows that the pressure distribution amplitude of the SFD decreases with increasing SFD clearance. When the SFD clearance is less than 0.14 mm, the pressure distribution amplitude of the SFD rapidly decreases, leading to a smaller range of liquid saturation vapor pressure and, thereby, to reduction of the extent of cavitation. However, when the SFD clearance exceeds 0.14 mm, the rate at which the pressure distribution amplitude of the SFD decreases slows down, and the occurrence of air ingestion becomes more prevalent with increasing SFD clearance, resulting in an increase of the extent of cavitation.

3.2. Damping characteristics

To investigate the effect of SFD clearance on the damping characteristics, different SFD clearances are selected: 0.08, 0.1, 0.12, 0.14, 0.16, 0.18 and 0.2 mm. The other SFD parameters are kept constant.

Figure 9 depicts the oil film pressure obtained through numerical simulations. In the axial direction, the amplitude of the positive pressure zone in the damper pressure distribution is high in the middle and low at both the ends. The amplitude of the negative pressure zone also exhibits the same pattern. Due to the presence of the oil supply hole, the pressure distribution exhibits fluctuations, and the waveform of the positive pressure zone is not completely smooth. Furthermore, the magnitude of pressure distribution decreases with increasing SFD clearance. When the SFD clearance is less than 0.14 mm, the magnitude of the pressure distribution rapidly decreases; when the SFD clearance exceeds 0.14 mm, the rate of decrease slows down. As the SFD clearance grows, the range of the positive pressure exhibits gradual transitions from 120°-

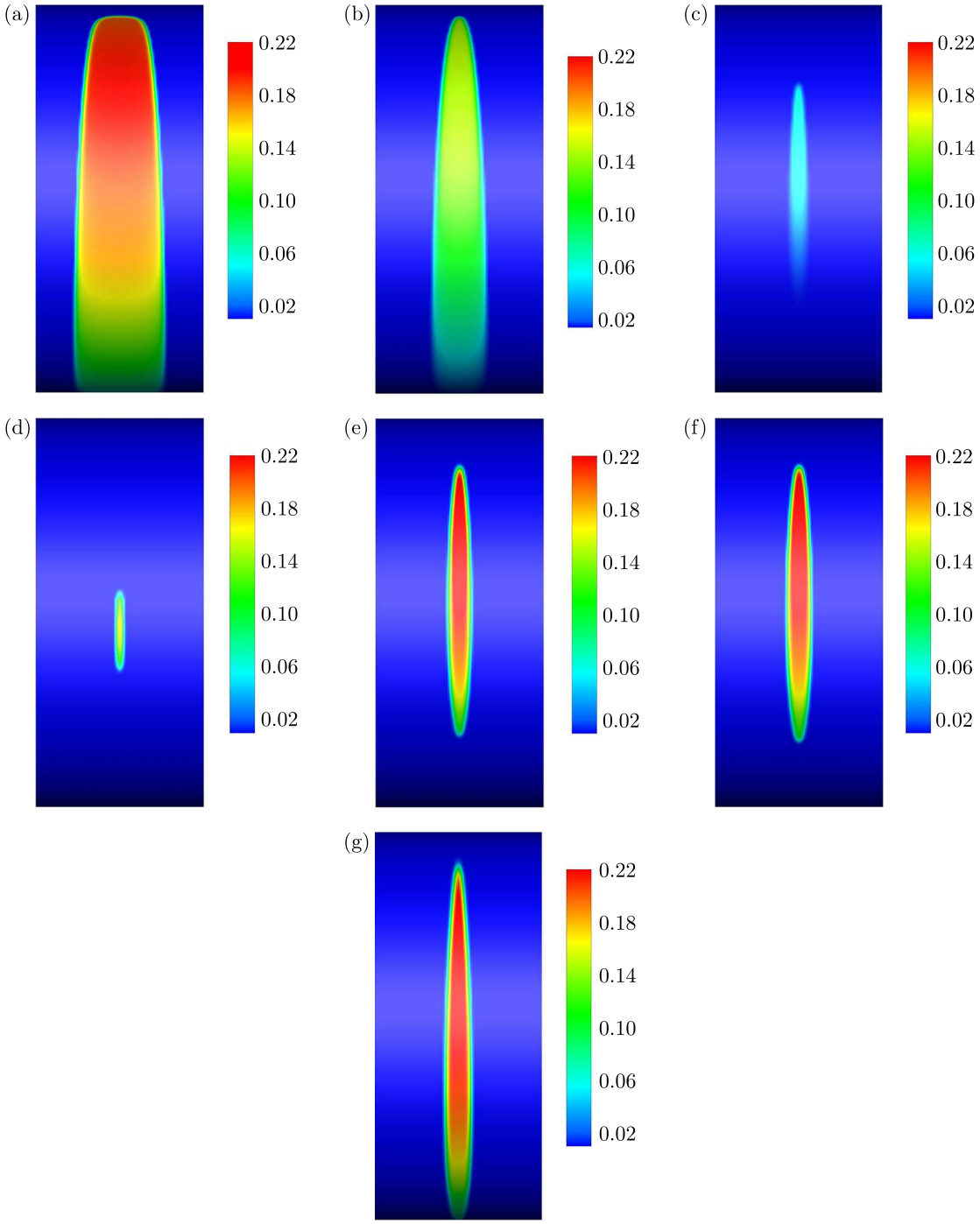

Fig. 8. Gas phase volume fraction range of SFDs with different clearances: (a) $c = 0.08$ mm, (b) $c = 0.1$ mm, (c) $c = 0.12$ mm, (d) $c = 0.14$ mm, (e) $c = 0.16$ mm, (f) $c = 0.18$ mm, (g) $c = 0.2$ mm

240° in the circumferential direction to 180°-360°, i.e., and the range of the positive pressure area expands.

Figure 10 presents the SFD stiffness and damping coefficients. Both coefficients decrease with increasing SFD clearance. When the clearance is less than 0.14 mm, the pressure distribution amplitude rapidly decreases, leading to a quick reduction in the SFD stiffness and damping coefficients. When the clearance exceeds 0.14 mm, the reduction rate of the pressure distribution amplitude and the stiffness and damping coefficients slow down.

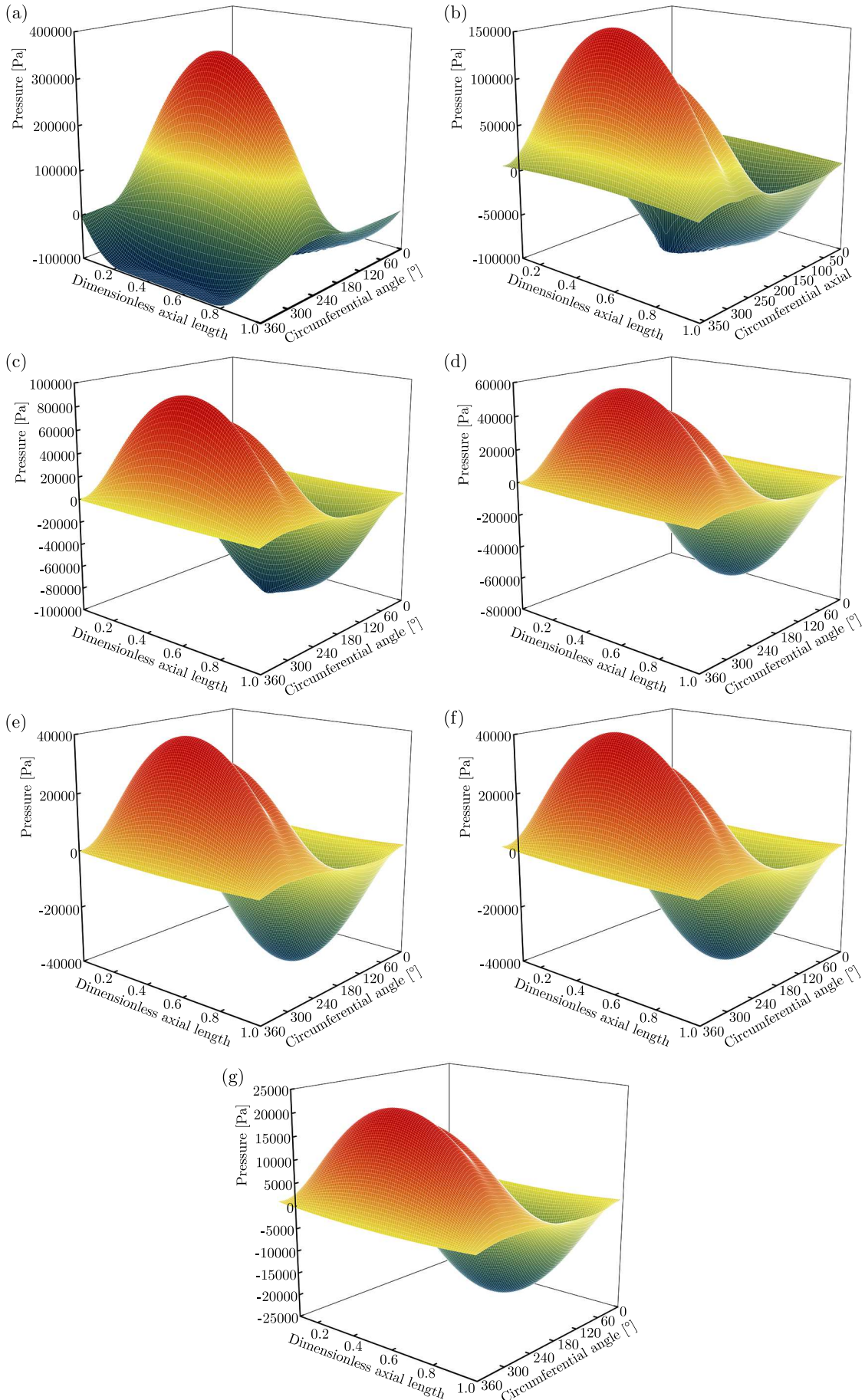

Fig. 9. SFD pressure distribution: (a) $c = 0.08\,\text{mm}$, (b) $c = 0.1\,\text{mm}$, (c) $c = 0.12\,\text{mm}$, (d) $c = 0.14\,\text{mm}$, (e) $c = 0.16\,\text{mm}$, (f) $c = 0.18\,\text{mm}$, (g) $c = 0.2\,\text{mm}$

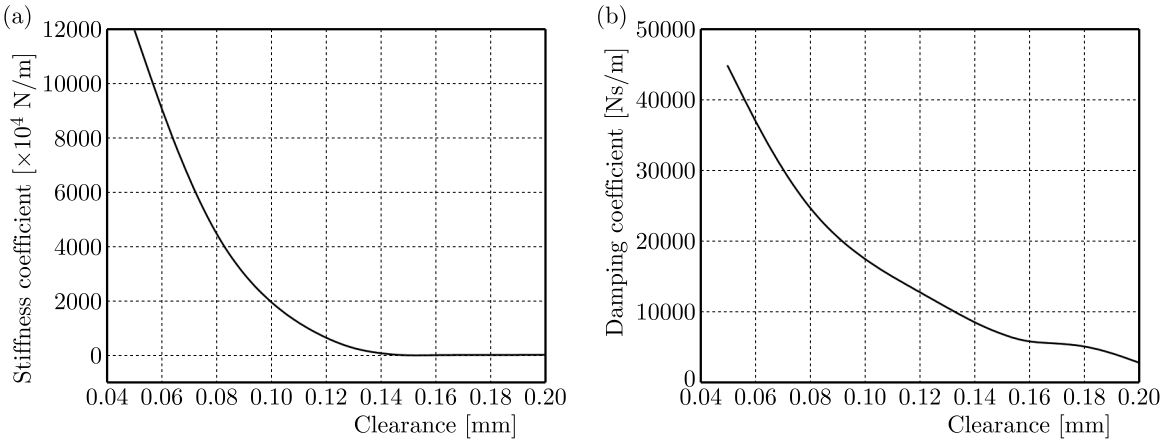

Fig. 10. (a) Stiffness and (b) damping coefficients

4. Dynamical characteristics of the rotor system

To investigate the influence of SFD clearance on the transient response of the rotor-SFD system, different clearances are selected: 0.05, 0.08, 0.1, 0.12, 0.14, 0.15, 0.16, 0.18 and 0.2 mm. The other damper parameters are kept constant. Figure 11 shows the transient responses of the elastic support of the rotor-SFD system under different clearances.

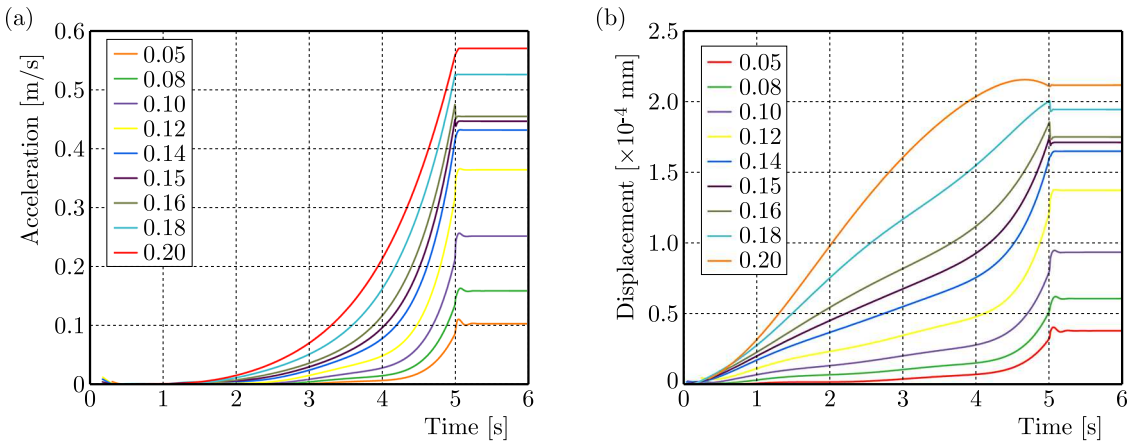

Fig. 11. Transient responses of the elastic support of the rotor-SFD system: (a) acceleration, (b) displacement

The figure depicts the acceleration and displacement response curves of the elastic support during the acceleration process of the rotor-SFD system from 0 rpm to 9000 rpm. The vibration amplitude of the rotor system increases with the SFD clearance. When the SFD clearance is less than 0.14 mm, the damping coefficient rapidly decreases, leading to a quick reduction in the vibration amplitude of the rotor system. Subsequently, the reduction rate of the vibration amplitude slows down. When the SFD clearance exceeds 0.16 mm, the rate of increase of the vibration amplitude accelerates. However, asynchronous displacement and acceleration amplitudes are observed.

5. Conclusions

This study established an SFD dynamic model considering both cavitation and fluid inertia, and analyzed the influence of SFD clearance on SFD cavitation and vibration reduction charac-

teristics. Moreover, a finite element model of the rotor-SFD system considering SFD damping characteristics was established. The influence of the SFD clearance on the transient response of the rotor-SFD system was studied. The accuracy of the dynamic model was experimentally verified. The following conclusions were obtained:

- The mismatch between the experimental and numerical simulation results was less than 5%, indicating that the numerical simulation method for the SFD and the finite element model of the rotor-SFD system proposed herein are reliable.
- When the SFD clearance was increased from 0.08 mm to 0.12 mm, both the extent of cavitation and the gas volume fraction decreased. As the SFD clearance exceeded 0.14 mm, the extent of cavitation expanded and the gas volume fraction gradually increased.
- The pressure distribution magnitude and the SFD stiffness and damping coefficients decreased with increasing SFD clearance. Additionally, the vibration damping effect of the SFD decreased.
- The vibration amplitude of the rotor system increased with the SFD clearance.

The proposed numerical simulation method of SFD allows for the study of the influence of structural and operating parameters of dampers on their vibration reduction characteristics, considering the effects of cavitation and inertia. Moreover, the finite element model of the rotor-SFD system presented in this study enables investigation of the influence of structural and operating parameters of the damper on the transient response of the rotor system. The proposed method enables better selection of the structural and operating parameters of an SFD during the design phase of the rotor system effectively reducing the vibration amplitude and improving stability of the rotor system during operation.

References

1. Chen H., Hou L., Chen Y., 2017, Bifurcation analysis of a rigid-rotor squeeze film damper system with unsymmetrical stiffness supports, *Archive of Applied Mechanics*, **87**, 8, 1347-1364
2. Crandall S.H., El-Shafei A., 1993, Momentum and energy approximations for elementary squeeze-film damper flows, *Journal of Applied Mechanics*, **60**, 3, 728-736
3. Drapatow T., Alber O., Woschke E., 2021, Transient simulation of a squeeze film damped turbocharger rotor under consideration of fluid inertia and cavitation, *Bulletin of the Polish Academy of Sciences-Technical Sciences*, **69**, 6, 1-8
4. El-Saeidy F.M.A., Sticher F., 2010, Dynamics of a rigid rotor linear/nonlinear bearings system subject to rotating unbalance and base excitations, *Journal of Vibration and Control*, **16**, 3, 403-438
5. El-Shafei A., 1991, Unbalance response of a Jeffcott rotor incorporating long squeeze film dampers, *Journal of Vibration and Acoustics*, **113**, 1, 85-94
6. El-Shafei A., 1995, Modeling fluid inertia forces of short journal bearings for rotordynamic applications, *Journal of Vibration and Acoustics*, **117**, 4, 462-469
7. El-Shafei A., 2002, A finite difference model for squeeze film dampers, *Journal of Engineering and Applied Science*, **49**, 1, 159-174
8. Fan T., Hamzehlouia S., Behdinan K., 2017, The effect of lubricant inertia on fluid cavitation for high-speed squeeze film dampers, *Journal of Vibroengineering*, **19**, 8, 6122-6134
9. Gehannin J., Arghir M., Bonneau O., 2016, A volume of fluid method for air ingestion in squeeze film dampers, *Tribology Transactions*, **59**, 2, 208-218
10. Gheller E., Chatterton S., Vania A., Pennacchi P., 2022, Squeeze film damper modeling: a comprehensive approach, *Machines*, **10**, 9, 1-26

11. Gupta R.K., Singh R.C., 2023, Comprehensive experimental analysis of a squeeze film damper for flexible rotor applications: utilizing Box-Behnken design with desirability optimization, *Journal of Vibration Engineering and Technologies*, **12**, 3, 5267-5290

12. Hamzehlouia S., Behdinan K., 2019, Squeeze film dampers supporting high-speed rotors: fluid inertia effects, *Proceedings of the Institution of Mechanical Engineers, Part J – Journal of Engineering Tribology*, **234**, 1, 18-32

13. San Andrés L., 1992, Analysis of short squeeze film dampers with a central groove, *Journal of Tribology*, **114**, 4, 659-664

14. San Andrés L., 2014, Force coefficients for a large clearance open ends squeeze film damper with a central feed groove: experiments and predictions, *Tribology International*, **71**, 17-25

15. Wang H., Zhao Y., Luo Z., Han Q., 2022, Analysis on influences of squeeze film damper on vibrations of rotor system in aeroengine, *Applied Sciences*, **12**, 2, 615

16. Younan A.A., Cao J., Dimond T.W., Allaire P.E.,, 2010, Nonlinear analysis of squeeze film damper with entrained air in rotordynamic systems, *Tribology Transactions*, **54**, 1, 132-144

17. Zapoměl J., Ferfecki P., Forte P., 2019, Vibrations attenuation of a Jeffcott rotor by application of a new mathematical model of a magnetorheological squeeze film damper based on a bilinear oil representation, *Acta Mechanica*, **230**, 1625-1640

18. Zhang M., 2018, *Simulation and Experimental Study on Dynamic Characteristics of Squeeze Film Damper* (in Chinese), Mechanical Engineering, Shenyang Aerospace University, Shenyang

19. Zhou H.L., Cang Y.G., Zhang Y.Q, Guo C., 2023, Analysis of dynamic characteristics of a sealed ends squeeze film damper considering the fluid inertia force, *Journal of Theoretical and Applied Mechanics*, **61**, 3, 441-452

20. Zhou H.L., Chen X., Zhang Y.Q., Ai Y.T., Sun D., 2020, An analysis on the influence of air ingestion on vibration damping properties of squeeze film dampers, *Tribology International*, **145**, 106168

Manuscript received March 30, 2024; accepted for publication September 14, 2024